Monthly Notices
of the
ROYAL ASTRONOMICAL SOCIETY

MNRAS **491,** 5586–5594 (2020) doi:10.1093/mnras/stz3260

Emission spectra of light-pollution sources determined from the light-scattering spectrometry of the night sky

Miroslav Kocifaj,[1,2]★ František Kundracik[2] and Ondrej Bilý[2]

[1]*ICA, Slovak Academy of Sciences, Dúbravská Road 9, 845 03 Bratislava, Slovak Republic*
[2]*Department of Experimental Physics, Faculty of Mathematics, Physics, and Informatics, Comenius University, Mlynská dolina, 842 48 Bratislava, Slovak Republic*

Accepted 2019 November 18. Received 2019 November 18; in original form 2019 June 24

ABSTRACT

The emission spectrum of a light-pollution source is a determining factor for modelling artificial light at night. The spectral composition of skyglow is normally derived from the initial spectra of all artificial light sources contributing to the diffuse illumination of an observation point. However, light scattering in the ambient atmosphere imposes a wavelength-specific distortion on the optical signals captured by the measuring device. The nature of the emission, the spectra and the light-scattering phenomena not only control the spectral properties of the ground-reaching radiation, but also provide a unique tool for remote diagnosis and even identification of the emission spectra of the light-polluting sources. This is because the information contained in the night-sky brightness is preferably measured in directions towards a glowing dome of light over the artificial source of light. We have developed a new method for obtaining the emission spectra using remote terrestrial sensing of the bright patches of sky associated with a source. Field experiments conducted in Vienna and Bratislava have been used to validate the theoretical model and the retrieval method. These experiments demonstrate that the numerical inversion is successful even if the signal-to-noise ratio is small. The method for decoding the emission spectra by the light-scattering spectrometry of a night sky is a unique approach that enables for (i) a systematic characterization of the light-pollution sources over a specific territory, and (ii) a significant improvement in the numerical prediction of skyglow changes that we can expect at observatories.

Key words: scattering – atmospheric effects – light pollution – methods: analytical – methods: numerical – methods: observational.

1 INTRODUCTION

Light emissions from artificial sources can make astronomical observations difficult because of the veiling luminance they produce as a result of light scattering by the night-time atmosphere (Narisada & Schreuder 2004). Inhabited areas produce, by far, the most light at night, from artificial light sources differing in size, shape, and spatial distribution, as well as in light output patterns (LOPs) or spectra. The latter two are important sources of uncertainty in skyglow modelling (Kyba et al. 2013a). LOPs (also referred to here as city emission functions, CEFs) have been systematically investigated in recent years (Kocifaj & Solano-Lamphar 2016; Solano-Lamphar 2018), and several tools have been developed to retrieve light-emission patterns from ground-based and/or aerial sensors (Kyba et al. 2013b; Kocifaj 2017; Kocifaj et al. 2019). The CEFs are obtained in natural units (e.g. relative to upward emissions) and can be calibrated against visible infrared imaging radiometer suite that supports day-night band (VIIRS-DNB) (see e.g. Duriscoe et al. 2014). However, it should be noted that satellite sensors are not very sensitive to blue light (Cao & Bai 2014), so emissions from LEDs are scarcely detected (Falchi et al. 2016). In many cases, the spectral composition of light escaping an urban area is only an estimate because the lighting inventory is largely incomplete or missing (with only a few exceptions, see e.g. Aubé et al. 2016 or Barentine et al. 2018).

The emission spectrum of all of a city's lights is a weighted contribution of the individual spectra, taking into account the prevailing technology of the outdoor lighting in the city (Bará et al. 2019). This is why the photons exiting an urban area carry information on the original emission spectrum. The methods for the characterization of a cloud of photons along their trajectories from the ground upwards are of great importance because they can provide vital data for optical diagnostics of bulk emissions from light-pollution sources. From this perspective, multispectral remote sensing from unmanned aircrafts, drones, helicopters, or

★ E-mail: kocifaj@savba.sk

balloons remains a huge technical and technological challenge (Cinzano & Falchi 2014; Barentine 2019). However, unlike the above-mentioned methods, the ground-based optical sounding of the night-sky brightness (NSB) appears to be a promising approach with significant economy and accuracy.

However, only a small fraction of the upward radiative flux returns to the ground surface under good astronomical observation conditions, namely a cloud-free sky and low atmospheric turbidity levels. The ability to capture the light on the ground improves as the distance to the light-pollution source decreases and when the photosensitive sensor is pointed towards the glowing dome of light. Independently of this, the atmosphere modulates, to some extent, artificial light before it is detected by the measuring device. The lives of photons of different wavelengths differ substantially because of the absorption and scattering processes in a turbid atmosphere (Bohren & Clothiaux 2006). Aerosol particles, which are small compared with the wavelength (or air molecules), scatter blue light intensively; thus the light becomes reddish in colour when transported on long optical paths (Cinzano, Falchi & Elvidge 2001; Aubé, Roby & Kocifaj 2013). The mathematical formula to model electromagnetic scattering from small particles is known as Rayleigh's law, which states that the intensity of scattered light is inversely proportional to the fourth power of wavelength (Kerola 2006; Kocifaj & Kómar 2016). This is why the scattering of red light is more than one order of magnitude less efficient than that of blue light; consequently, long-range transport of blue light is, in general, difficult. However, those natural aerosols that are comparable to, or larger than, the wavelengths of visible radiation perturb this simple power law (Kokhanovsky & Zege 1997), thereby making scattering phenomena more complex (Kocifaj 2018).

In this paper, we have developed, and experimentally validated, a new method for obtaining the emission spectra of a light-pollution source from a remote terrestrial sensing of the dome of light that is over the light source. The experiments were conducted near a town or city. This is preferable because (i) we can avoid parasitic effects from other cities, (ii) contributions from artificial sources other than the NSB (e.g. the oxygen line at 557.7 nm) are significantly suppressed, and (iii) simple low-cost spectrometers can be used to retrieve the emission spectrum. The emission spectrum is then used as an input to the numerical models to predict spectral changes to the NSB from variable turbidity conditions at any point in the city's surroundings (e.g. at or near distant observatories). The emissions from a set of cities/towns can be combined to model the cumulative effects on the NSB spectra from all important sources of light. Because of its simplicity, the method can be applied to most artificial light sources. The numerical implementation of the retrieval algorithm is now publicly available (Kundracik 2019), and the concept of the solution is described below.

2 SPECTRAL DISTORTION OF EMISSION SPECTRA OWING TO ATMOSPHERIC LIGHT SCATTERING

In the absence of clouds, the night-sky radiance $I(z)$ is proportional to the integral product of the atmospheric volume scattering coefficient $k_{\rm sca}$ and the transmission coefficient T (Kocifaj 2007), modulated by the geometrical factor $(\cos z_0/h)^2$. In other words,

$$I\left(z\right) \propto \frac{Q_0}{\cos z} \int_0^\infty \left(\frac{\cos z_0}{h}\right)^2 T\left(h, z, z_0\right)\ k_{\rm sca}\left(h, \theta\right)\ {\rm d}h, \tag{1}$$

where z is the observational zenith angle, h is the altitude above ground level, and z_0 is the zenith angle of light emissions from a ground-based source with a total power output of Q_0. Normally, Q_0 is determined by the spectral range of all contributing sources of light. However, it is modified by the sensor's spectral sensitivity function, which is superimposed on the spectrum of the night-sky light. The use of interference filters, or even diffraction grating spectrometers, allows for narrowband radiometry when photons with different wavelengths hit different pixels of the detector. Spectral measurements are advantageous as they permit signal analysis for equally sized and uniformly spaced wavelength intervals (usually of a few nanometres), independent of the widths and shapes of the spectra of all contributing city lights. The physical meaning of the volume scattering coefficient $k_{\rm sca}(h,\ \theta)$ is explained by Horvath (2014), who uses the symbol γ instead of our $k_{\rm sca}$. The function we have introduced has units of $\mathrm{m^{-1}sr^{-1}}$ and includes the vertical stratification of light-scattering atmospheric constituents, specifically Rayleigh scatterers (air molecules) and particulate matter (aerosols). This function is given by

$$k_{\rm sca}\ (h, \theta) = \frac{1}{4\pi}\ \left[k_{\rm R}\left(h\right) P_{\rm R}\left(\theta\right) + k_{\rm A}\left(h\right) P_{\rm A}\left(\theta\right)\right], \tag{2}$$

where $k_{\rm R}(h)$ and $k_{\rm A}(h)$ are the Rayleigh and aerosol scattering coefficients measured in $\mathrm{m^{-1}}$, which can be derived from the respective cross-sections (Rozanov et al. 2014). By analogy, $P_{\rm R}(\theta)$ and $P_{\rm A}(\theta)$ are the Rayleigh and aerosol scattering phase functions, both normalized to 4π. The physical interpretation of the transmission coefficient T is that it is the optical transparency along the beam path from the light source to the detector (see e.g. Louedec et al. 2012 for the aerosol transmission coefficient and beams propagated along an inclined trajectory).

The elevated brightness of the dome of light over a city is primarily due to two effects: (i) the small-angle scattering in the turbid atmosphere supports a rapid increase in scattering amplitudes (i.e. the intensity of scattered light); and (ii) the peak concentration of atmospheric constituents in the lower atmosphere is manifested through an enhanced scattering efficiency. The turbulent mixing processes cause the concentrations of atmospheric contaminants to not decrease with altitude in the atmospheric boundary layer (Haeffelin et al. 2012). For these reasons, and also because $T \approx 1$ for a beam of light transported over short optical paths (when the dome of light over a light-pollution source is remotely sensed at a physically short distance D), the $k_{\rm sca}(h, \theta)$ can be replaced by $k_{\rm sca}(\theta)$. After some manipulation, the derivative dh can be expressed as

$${\rm d}h = -\frac{h^2}{D}\frac{dz_0}{\cos^2 z_0}\ , \tag{3}$$

so the integration in equation (1) simplifies to

$$I\left(z\right) \propto \frac{Q_0}{\cos z}\frac{1}{D}\int_{-z}^{\pi/2}\ k_{\rm sca}\left(\theta\right)\ {\rm d}z_0, \tag{4}$$

where the emission zenith angle z_0 ranges from $-z$ (which is the detectable limit for beams emitted at azimuth angles opposite to the position of an observer) to $\pi/2$ (for upward flux at angles near the horizontal). The scattering function in polluted air is a linear combination of Rayleigh scattering, which is front–back symmetric, and aerosol scattering, for which the scattering pattern is dominated by the forward lobe. There are a number of works demonstrating that the scattering pattern approximated by the Henyey–Greenstein (HG) function closely resembles the true phase function, except for aerosols of size comparable to, or larger than,

liquid cloud droplets (Li et al. 2015). The HG function usually mimics the angular distribution of the scattered light for spherical Mie particles adequately (Moosmüller & Ogren 2017). However, the HG function can also be applied to other morphologies if the scattering angle is low. This is because the scattering from spherical and that from spheroidal particles are similar for small angles (Fu et al. 2009). The volume scattering coefficient can then be expressed as

$$k_{\rm sca}\ (\theta) = \frac{k_{\rm R}}{4\pi}\,\frac{3}{4}\left(1+\cos^2\theta\right) + \frac{k_{\rm A}}{4\pi}\,\frac{1-g^2}{\left(1+g^2-2g\cos\theta\right)^{3/2}}, \quad (5)$$

where the asymmetry parameter g shapes the HG function. The photon distribution is isotropic when $g = 0$. The positive values of g indicate that the scattering in a forward direction exceeds that in a backward direction. The particles that scatter preferably backwards have $g < 0$. The value of g cannot be smaller than –1 (reflective media) or larger than 1 (forward scatterers) (Hanafy, Roggemann & Guney 2014).

Assuming that observations are made along the bisectrix of the directions to the two light-dome edges (i.e. the line-of-sight crosses the dome of light at its brightest point, with the angular distances from the two edges nearly equal), equation (4) transforms to

$$I\,(z) \propto Q\,i_{\rm R}\,(z) + Q\,i_{\rm A}\,(z)\,, \quad (6)$$

where

$$i_{\rm R}\,(z) \propto \frac{\tau_{\rm R}}{\cos z}\,\frac{3}{16\pi D}\int_{-z}^{\pi/2}\left[1+\cos^2\left(\pi-z-z_0\right)\right]\,{\rm d}z_0 = \frac{\tau_{\rm R}}{\cos z}\,\frac{3}{16\pi D}\left(\frac{\pi}{4}+\frac{z}{2}+\frac{\sin 2z}{4}\right) \quad (7)$$

and

$$i_{\rm A}(z) \propto \frac{\tau_{\rm A}}{\cos z}\,\frac{1}{4\pi D(1-g)}\left\{E\left(\frac{\pi}{4}+\frac{z}{2},\,\frac{4g}{(1+g)^2}\right) - E\left(\frac{z}{2},\,\frac{4g}{(1+g)^2}\right)+\frac{2g}{(1+g)} \times\left[\frac{\sin z}{\sqrt{1+g^2+2g\cos z}}-\frac{\cos z}{\sqrt{1+g^2-2g\sin z}}\right]\right\}. \quad (8)$$

Here, the volume scattering coefficients $k_{\rm R}$ and $k_{\rm A}$ are linearly proportional to the optical depths $\tau_{\rm R}$ and $\tau_{\rm A}$ for Rayleigh and aerosol scattering, respectively. Therefore, $\tau_{\rm R}$ is replaced by $k_{\rm R}$ in equation (7), and $\tau_{\rm A}$ is replaced by $k_{\rm A}$ in equation (8). In addition, our numerical computations for a wide range of input parameters have demonstrated that the theoretical radiance is dominated by the scattering angle $\theta = \pi - z - z_0$ thanks to the symmetry of the relationships. The function

$$E\ \left(\varphi, x^2\right) = \int_0^{\varphi}\sqrt{1-x^2\sin^2\vartheta}\ {\rm d}\vartheta \quad (9)$$

used earlier is the incomplete elliptic integral (Fukushima 2011; Byrd & Friedman 2013). The Rayleigh optical depth $\tau_{\rm R}$ in equation (7) is easy to compute for a specific wavelength λ or for a spectral band by taking advantage of the formula $\tau_{\rm R} = 0.00879\lambda^{-4.09}$, where λ is in micrometres. A common approach to modelling $\tau_{\rm A}$ is to use a power-law function $\tau_{\rm A} = \tau_{\rm A0}(\lambda/\lambda_0)^{-\alpha}$, where $\tau_{\rm A0}$ is the aerosol optical depth at the nominal wavelength λ_0 and α is the Ångström wavelength exponent, which normally fluctuates around unity (Pepijn et al. 1999; Carretas Wagner & Janeiro 2015). The asymmetry parameter g can be inferred from information on

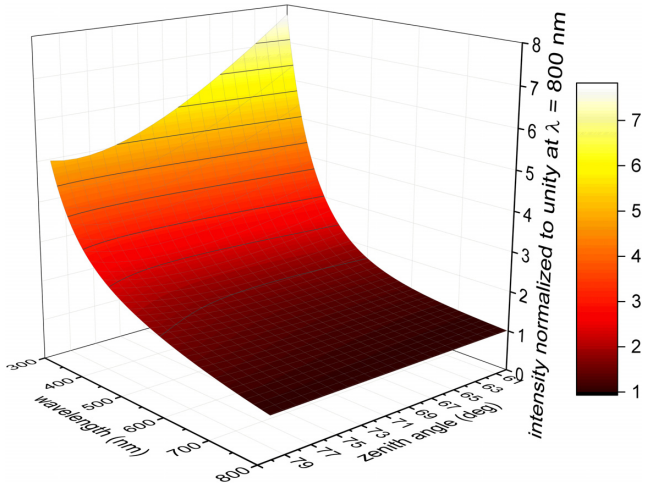

Figure 1. The theoretical brightness of a glowing dome of light is normalized to unity at $\lambda = 800$ nm. The input data to the model are as follows: $\tau_{\rm A0}$= 0.4 at $\lambda = 500$ nm, the Ångström wavelength exponent $\alpha = 1$, and the scale parameters for the particle size distribution function are: $a = 2$, $b = 20\ \mu{\rm m}^{-1}$ (i.e. the modal radius is 0.1 μm).

the locality and local sources of air pollution. For instance, small particles that are typically found at high altitudes (e.g. in mountain regions) support low values of g, while particles comparable to or larger than the wavelengths of the visible spectrum have $g > 0.5$ (see e.g. fig. 9a in Cappa et al. 2016 or fig. 1 in Moosmüller & Ogren 2017). Kocifaj (2011) has shown that an asymmetry parameter can also be estimated from the number size distribution function of the aerosol particles, $f(r)$, using the approximate formula $g = \cos^2 G(a,\ \lambda b)/[1+G^2(a,\ \lambda b)]$, where a and b are parameters that control $f(r)$. The term $G\ (a,\ \lambda b) = \frac{10\gamma^2+\lambda b}{8\pi}\,\frac{8}{10+5a(\gamma\pi)^{-2}}$ where $\gamma = 0.577$ is the Euler constant. The parameter a is related to the parameter b through the modal radius $r_{\rm m} = a/b$, which is known as the most common radius in populations of aerosol particles.

Fig. 1 provides an insight into how the night-sky brightness (NSB) above a city depends on λ. In this figure, the observational zenith angle, z, ranges from roughly 60° to 80°, while the NSB is normalized to unity at $\lambda = 800$ nm in order to better see the relative increase of $I(z)$. Fig. 1 demonstrates that the relative blue light contribution to the NSB increases when transitioning from high to low zenith angles, that is, when the angle above the horizontal increases. It also means that a glowing dome of light becomes redder near the horizon and bluer far from the horizon. This can be interpreted as the transition from aerosol-controlled NSB at low elevation angles to an increased Rayleigh scattering contribution to the NSB at high elevation angles. Undoubtedly, the loss of blue light significance near the horizon is due to the fact that the aerosol scattering pattern is forward-lobed (Li et al. 2019). The intensity of light scattered by aerosol particles at small scattering angles normally exceeds the Rayleigh scattering intensity by a factor of 10–100 (see e.g. fig. 5 in Horvath 2014; fig. 6 in Mayer & Kylling 2005) or even more – particularly if the particles are as large as water droplets (fig. 3 in Davis & Marshak 2010). Therefore, the nature of the spectral distortion of artificial-source emissions depends on the aerosol sizes and on the asymmetry parameter g.

3 METHOD TO DETERMINE THE EMISSION SPECTRUM OF A LIGHT-POLLUTION SOURCE

Equation (6) can be used in the spectral transform analysis as it provides a mapping from emission spectra $Q(\lambda)$ to NSB spectra $I(z,\ \lambda)$ and vice versa. The inverse transform has the form

$$Q\left(\lambda\right) \propto \frac{I\left(z,\lambda\right)}{i_{\mathrm{R}}\left(z,\lambda\right)+i_{\mathrm{A}}\left(z,\lambda\right)}. \tag{10}$$

The spectrum $Q(\lambda)$ implicitly includes contributions from all types of light sources to the light escaping a city (reflected light is included). The urban area is a heterogeneous environment occupied by obstacles of different shapes and optical properties. The multifaceted interactions between artificial light and these obstacles make the directions and optical properties of reflected light difficult to predict. Therefore, there is nothing intrinsically unusual about reflected light containing a non-trivial combination of manifold interactions of artificial light with all types of surfaces, each having a different spectral reflectivity. This is why the average ground albedo is preferred, in various studies, to characterize an urban environment (Chimklai, Hagishima & Tanimoto 2004 or Yang & Li 2015). With this concept, the relative shape of the spectrum for the reflected component of $Q(\lambda)$ is fully consistent with that of the total $Q(\lambda)$, meaning that the addition of reflected light to the direct emissions (from e.g. streetlights) has a small or zero impact on the spectral composition of light escaping a city. Thus, the monitoring of $Q(\lambda)$ allows for an approximate characterization of the whole-city light sources.

Owing to experimental errors, equation (10) is only an approximation to the emission spectra. One procedure to determine the emission spectrum with greater accuracy is to use basis functions associated with the true spectra of real lighting technologies. The true solution must be a linear combination of one or more light-type spectra that together produce the spectrum closest to $Q(\lambda)$, while also taking into account experimental errors. This method is described in the subsequent sections.

3.1 NSB spectral decomposition into basis functions

The key idea behind the retrieval of the true emission spectrum is to write $Q(\lambda)$ as a linear combination of the real spectra of different types of lighting technologies. Spectra that differ only in a few features cannot form the space of basis functions (see Section 3.2). However, if the basis functions f_i are properly selected, it should be possible to express the experimentally determined $Q(\lambda)$ as

$$Q\ \left(\lambda\right) = c_1\ f_1\left(\lambda\right) + \ c_2 f_2\left(\lambda\right) + \cdots c_k f_k\left(\lambda\right) + \varepsilon\left(\lambda\right), \tag{11}$$

where $\varepsilon(\lambda)$ is a random error with a specific error margin. Assuming that measurement errors have a Gaussian distribution, a set of coefficients c and basis functions f that best match n-dimensional data-vector $Q(\lambda_i)$ $(i\ =\ 1...n)$ can be obtained by minimizing the functional

$$\sum_{i\ =\ 1}^{n}\left\{Q\left(\lambda_i\right) - \left[c_1 f_1\left(\lambda_i\right) + \ c_2 f_2\left(\lambda_i\right) + \cdots c_k f_k\left(\lambda_i\right)\right]\right\}^2, \tag{12}$$

where n is the number of sampled wavelengths in the NSB spectrum and $Q(\lambda_i)$ is computed from equation (10) for λ_i. The solution vector $\boldsymbol{c}$ for a selected set of basis functions $\boldsymbol{y}$ can be obtained from

$$\boldsymbol{c} = \left(\overline{\overline{X}}^{\mathrm{T}}\overline{\overline{X}}\right)^{-1}\ \left(\overline{\overline{X}}^{\mathrm{T}}\boldsymbol{y}\right), \tag{13}$$

where

$$\boldsymbol{c} = \begin{pmatrix} c_1 \\ c_2 \\ \cdots \\ c_k \end{pmatrix}\ \boldsymbol{y} = \begin{pmatrix} f(\lambda_1) \\ f(\lambda_2) \\ \cdots f(\lambda_n) \end{pmatrix}$$

$$\overline{\overline{X}} = \begin{pmatrix} f_1(\lambda_1) & f_2(\lambda_1) & \cdots & f_k(\lambda_1) \\ f_1(\lambda_2) & f_2(\lambda_2) & \cdots & f_k(\lambda_2) \\ \cdots & \cdots & \cdots & \cdots \\ f_1(\lambda_n) & f_2(\lambda_n) & \cdots & f_k(\lambda_n) \end{pmatrix}. \tag{14}$$

The sample standard deviation is computed using the formula

$$u^2\ \left(c_j\right) = \left\{\left(\overline{\overline{X}}^{\mathrm{T}}\overline{\overline{X}}\right)^{-1}\right\}_{jj} u^2, \tag{15}$$

where

$$u^2 = \frac{\sum_{i=1}^{n}\left\{Q\left(\lambda_i\right) - \left[c_1 f_1\left(\lambda_i\right) + \ c_2 f_2\left(\lambda_i\right) + \cdots c_k f_k\left(\lambda_i\right)\right]\right\}^2}{n-k}. \tag{16}$$

We note that the success of the spectral decomposition depends on the proper selection of the basis functions.

3.2 Generating a basis function set

The best conditions are achieved when the lighting technologies used in a city are known and we only need to search for their relative contributions to the bulk light emissions. In such cases, the set of basis functions is given (and fixed), and thus determining the spectral decomposition is a straightforward task. However, selection of the base set is not usually as easy, for several reasons, as follows.

(i) Depending on the manufacturer, the same light-source types may differ slightly in their spectral features. For instance, different LEDs may show slightly different blue or green shifts of the spectral peak position. Metal halide lights contain heavy metal vapours, and different mixtures of gases can influence the emission spectrum.

(ii) The complete lighting inventory for a city is difficult to ascertain because ownership of light sources is very complex and difficult to establish.

(iii) Same-type light sources with different power consumptions normally have similar, but not necessarily identical, relative intensity distributions in their emission spectra; thus, the matrix $\overline{\overline{X}}^{\mathrm{T}}\overline{\overline{X}}$ is nearly singular. This implies that the computation of c_j may fail.

(iv) In most cases, the spectral resolution of the measured NSB is not as high as that of the basis functions, so the peaks in a measured spectrum may appear not as high and not as narrow as those identified in basis functions.

The basis functions we have created are derived from the LICA-UCM lamps spectral data base (Tapia Ayuga & Zamorano 2018; Tapia Ayuga et al. 2019). However, the spectra of same-type light sources (e.g. high-pressure sodium lamps) were grouped together and averaged with the aim of emphasizing the features that are common among all of these sources and of suppressing those spectral features that can only rarely be found in a selected group. The list of the averaged basis functions we have created in this way is referred to here as the 'generic spectra' and contains the following

elements: high-pressure sodium (HPS) lamps, low-pressure sodium 1701 K Lica (LPS) lamps, fluorescent lamps (FL), compact fluorescent lamps (CFL), metal halide (MH) lamps, ceramic metal halide (CMH) lamps, halogen 2911 K Lica Philips (H) lamps, incandescent tungsten 2805 K Lica Philips (I) lamps, LED streetlamps: LED 1833K-2877K, LED 2958K-3969K, LED 4225K-9089K, LED 23223K-25000K. The use of lower-correlated color temperature (CCT) LEDs results in less artificial sky brightness, at least in environments with low aerosol content, which are typical of dark-sky locations where major observatories are located. The list can be expanded or modified at any time, if needed. For instance, incandescent tungsten lights are used infrequently, for example in historical city centres, but most of them are currently being replaced by modern technologies. In addition, the ground-albedo-weighted components of the above spectra can be incorporated into the model if the types of dominant surfaces are known. In this way, the list can be extended by adding reflection spectra superimposed on the 'generic spectra'.

3.3 Raw spectra conversion and correction

Our intention when using generic spectra is to identify the dominant technologies rather than to distinguish between light sources of the same type that differ only insignificantly in their spectra. Therefore, we first split the measured spectrum into evenly spaced and equally sized intervals of width $\Delta\lambda$ and integrated the signals detected within each of these narrow-band cells. The scalar values we obtained for all intervals constructed a new vector of data-function that was useful for further numerical analysis. This procedure largely suppresses differences between the spectral signatures of the same-type lights. However, the proper choice of $\Delta\lambda$ is the decisive factor in the identification of participating lighting technologies. Specifically, $\Delta\lambda$ must satisfy the following requirements.

(i) For intervals $\Delta\lambda$ smaller than $\Delta\lambda_0$, the differences between computed and measured spectra (here referred to as residuals) show systematic deviations from the normal distribution, while $\Delta\lambda > \Delta\lambda_0$ tends to produce a normal distribution of errors. The optimum value of $\Delta\lambda_0$ has to be found numerically (e.g. by using the Shapiro–Wilk test of normality, see below).

(ii) The standard deviation of u^2 decreases as the wavelength width $\Delta\lambda$ increases. In this case, the spectrum exhibits some typical features. When $\Delta\lambda$ increases further, the u^2 gradually reaches its minimum (or remains constant) and then asymptotically increases, in most cases.

(iii) The coefficients c_j remain virtually unchanged when $\Delta\lambda$ are close to $\Delta\lambda_0$.

The Shapiro–Wilk test of normality was used to validate the residuals. We implemented the concept of the probability value or significance (p-value) to test whether the normally distributed residuals are obtained with a specified confidence. For p-values above 0.05, the confidence interval covers 95 of 100 cases (we emphasize that, in this study, the p-values are below 0.05 when the distribution of errors deviates from normal). The method to determine the proper value of $\Delta\lambda_0$ was validated with the data recorded in 2010, in Bratislava (see Section 4), and the HPS, FL, MH and tungsten lamps were initially selected as basis functions for the city. We found that the residuals are random with normal distributions for $\Delta\lambda > 19$ nm (see Fig. 2). Therefore, the optimum value of $\Delta\lambda_0$ is 20 nm, but this does not mean that any value of $\Delta\lambda$ above $\Delta\lambda_0$ is appropriate for the identification of lighting. For instance, $\Delta\lambda = 21$ nm, used for Bratislava, produces a p-value

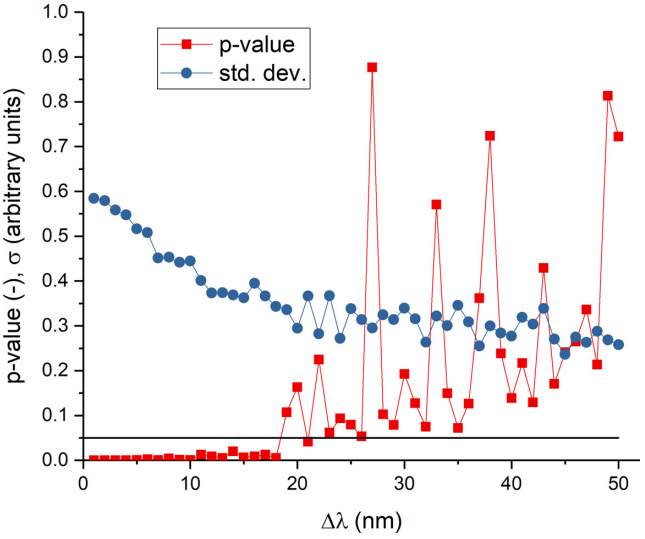

Figure 2. Standard deviation (blue circles) of u^2 (equation 16) and p-value (red squares) for the experimental data taken near the city of Bratislava. The critical p-value of 0.05 is shown as a horizontal solid line.

lower than 0.05; thus, we need to investigate other values of $\Delta\lambda$ around 21 nm. Such a test has to be performed on each new set of NSB data. Fortunately, this procedure is extremely fast and does not involve any additional numerical burden. Basically, the test should also yield c_j that do not change much with $\Delta\lambda$.

3.4 The method to reveal the relative contributions of dominant light types

The coefficients c_j can be interpreted as weights for the basis functions in formula (11). However, the relative contributions of $P_{m\,=\,1..k}$ of different light types to the emission spectra need to be calibrated as follows:

$$P_m\ (\%) = \frac{p_m}{\sum_{j=1}^{k} p_j}\ 100\%, \tag{17}$$

where the index $m\ =\ 1 \ldots k$ is used to number the basis functions, and

$$p_m = c_m\ \int_{\lambda_{\rm MIN}}^{\lambda_{\rm MAX}} f_m\,(\lambda)\ \nu\,(\lambda)\ {\rm d}\lambda. \tag{18}$$

The wavelengths $\lambda_{\rm MIN}$ and $\lambda_{\rm MAX}$ define the actual spectral range in which the optical device (spectrometer) is operated. Assuming that a filter with a spectral transmittance of $\nu(\lambda)$ is mounted in front of a photosensitive sensor, equation (18) also allows us to calculate p_m for $\nu(\lambda)$, being identical to the perception of the human visual system. Otherwise, $\nu(\lambda)$ is set to 1 to simulate a fully uncovered sensor.

4 EXPERIMENTAL RESULTS AND VALIDATIONS

The spectra recorded during the two field experiments in Slovakia and Austria were used to validate the method that we have developed. Novák, Sokanský & Diviš (2011) measured the night-sky spectrum at Patrónka on 2010 December 8, at 18:30, shortly after the beginning of the astronomical night (at Sun altitude −24°). The data were for the western part of Bratislava, where HPS lamps dominate over all other light sources. The tall buildings in this area also produce visible light owing to emissions from fluorescent

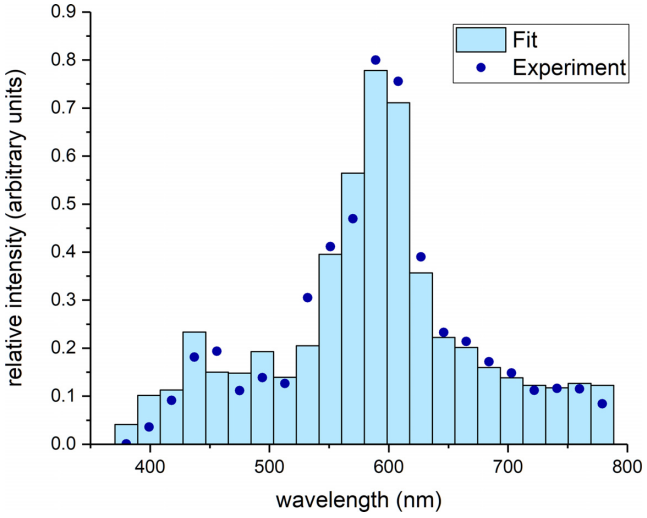

Figure 3. NSB spectrum measured in Bratislava (blue dots) versus the results of numerical inversion using the method introduced in Sections 3.1–3.4 (Fit). The spectrum recorded by Novák et al. (2011) has been scaled down to a resolution of 19 nm.

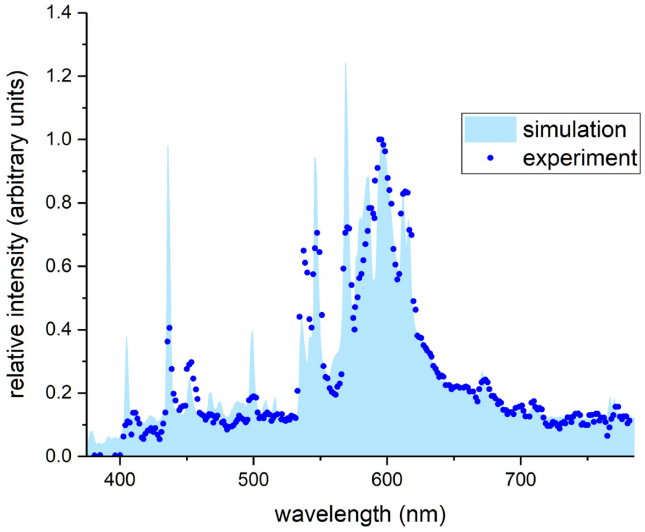

Figure 4. The high-resolution NSB spectrum measured in Bratislava is indicated with blue dots (compare with the low-resolution spectrum shown in Fig. 3). The continuum spectrum with a few sharp peaks is computed as a superposition of HPS, FL, MH and H, taking into account the relative weights we determined from numerical inversion.

lamps, while their facades are illuminated mostly by metal-halide sources. The experiment was conducted in overcast sky conditions to avoid spectral distortion due to aerosol and Rayleigh scattering phenomena. This allowed us to exclusively validate the method independently of light-scattering effects because the spectral power distribution is more or less conserved in the process of diffuse reflection from clouds (see e.g. fig. 2 in Dong 2018), and the optical transmission coefficients are close to unity when the beams of light are transported along short optical paths from the source of light to the measuring device. The spectral transformation in terms of equation (10) was therefore omitted, and the numerical processing includes the method described in Sections 3.1–3.4. The optimum spectral width of $\Delta\lambda = 19$ nm (discussed earlier) was used in the numerical processing of the experimental data. The results we obtained were compared against the original night-sky spectrum but scaled down to a resolution of 19 nm. The blue dots in Fig. 3 are used for the spectrum measured by Novák et al. (2011), while the bins are used for the results we obtained from our numerical inversion of the NSB. Here, the NSB is the intensity and is shown in arbitrary units. The use of arbitrary units throughout the paper is advantageous mainly because we evaluate the relative contributions of light sources with different spectral power distributions to the emission spectrum of the whole-city lights. The shapes of the relative spectra obtained here from the numerical inversion are independent of whether the experimental data are provided in relative or absolute units. Furthermore, the use of arbitrary units is advantageous because we do not need to recalibrate the radiometer against a standard source of light. In addition, we do not need the calibration to account for the ageing of any optical components. It is important to note that the NSB provided in 'arbitrary units' is linearly proportional to the NSB measured in basic SI units (W m^{-2} nm^{-1} sr^{-1}).

The relative contributions of lighting technologies that we derived from the NSB spectra are basically in line with what we know from the inventory of local light sources in the area of Patrónka. HPS was found to be the dominant source of light, with a relative contribution to the total emission of 42 per cent (±5 per cent). Other light sources we found in the spectra are: FL (22 per cent with an uncertainty of ± 3 per cent), MH (21 per cent, ±6 per cent), and H (15 per cent, ±4 per cent – most probably due to heavy traffic at Patrónka crossroads, even at night). Considering that the measurements were taken shortly after the beginning of the astronomical night, the large contribution from FL is most likely due to light emissions from the interior. The above distribution of the most important types of city lights permits a modelling of the high-resolution emission spectrum as a superposition of all contributing lighting technologies, taking into account their relative weights. To do this, we used the data base of generic spectra that we had created earlier. The simulated versus measured high-resolution spectra are shown in Fig. 4.

Another experiment we used to validate our method was that performed by Puschnig, Posch & Uttenthaler (2014) at the Vienna University Observatory on 2012 February 1 (time information not provided). The spectroscopic observations they made using an 80-cm Cassegrain telescope revealed emission lines that correlated with FL (which is expected to be a common type of light in residential areas) and HPS (which is used for street-lighting in the area surrounding the measuring site). We analysed the original spectrum taken in Vienna and used the same algorithm as above. In the relative contributions of the most prominent types of light, FLs dominate with a 46 per cent incidence rate, followed by HPS lights (19 per cent) and H lights (35 per cent). The uncertainties in the numerically obtained fractions of the whole are ±2 per cent for all of the above light types. We stress that the halogen lights (H) emitted strongly at the red edge of the visible spectrum. The lumen output they produced was small, although the total power output was as high as 35 per cent. Although the time information is missing, and we do not know if the spectrum characterizes the night sky before or after midnight, the large contribution from FLs may be due to the fact that the public lighting operated for the whole night. Puschnig et al. (2014) argue that 80 per cent of all the lamps used for public lighting in Vienna are FLs (most often of the type T-8, which is included in the generic spectra). Therefore, the results we obtained are consistent with what we expected. Fig. 5 demonstrates how well our inverse transform reproduces the measured spectra.

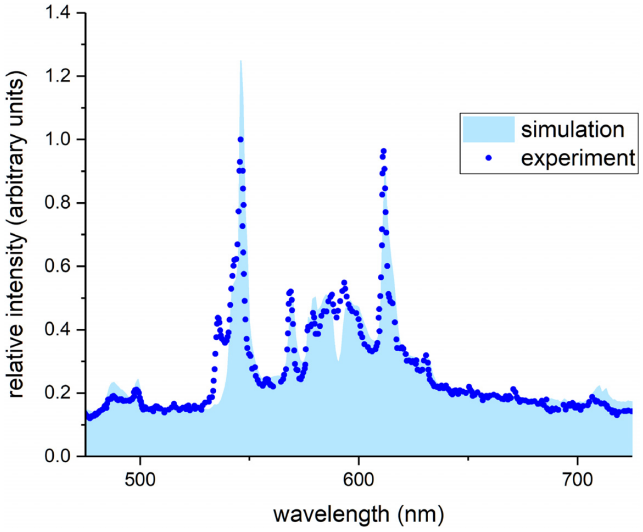

Figure 5. The spectrum of the Viennese night sky taken by Puschnig et al. (2014, blue dots) is satisfactorily reproduced by the theoretical model developed in this paper (simulation).

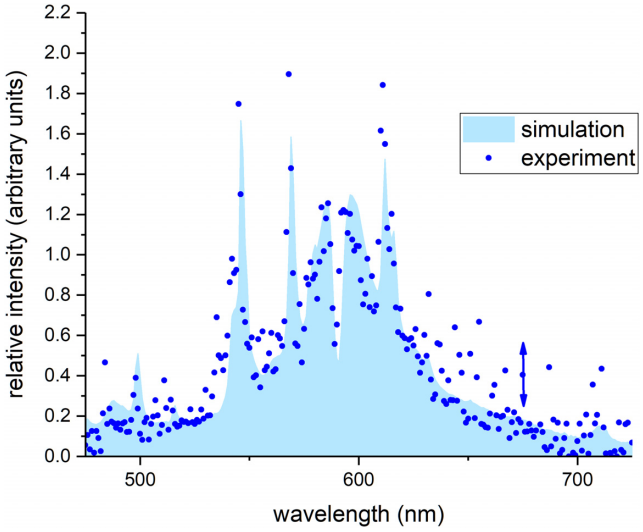

Figure 6. The spectrum of a night sky taken in Kagran (Vienna) in 2018 (experiment, blue dots) and the simulated spectrum (simulation). The differences are due to a low signal-to-noise ratio; however, the theoretical model succeeded in identifying key spectral features. The double arrow (vertical error bar) indicates the average noise magnitude.

The model validation process for the two independent experiments was supplemented by a field experiment in Vienna, which was conducted under clear sky conditions on 2018 November 19, at 21:45 local time. The night-sky radiance was taken in Kagran (8 km north of the city centre of Vienna) 30° above the horizon. The bright dome of light we observed allows for the use of a simple device based on the USB-650 Red Tide class of Ocean Optics Spectrometers. Despite the dark spectrum reduction, the signal-to-noise ratio was still not as good as required. The noise vanished slowly with increasing exposure time, up to its maximum (30 s). The noise had a negative impact on the accuracy of the numerical inversion, as shown in Fig. 6. This is why the error margins of 5–9 per cent for the dominant types of light-pollution sources are relatively large: HPS, 36 ± 5 per cent; FL, 34 ± 5 per cent; and

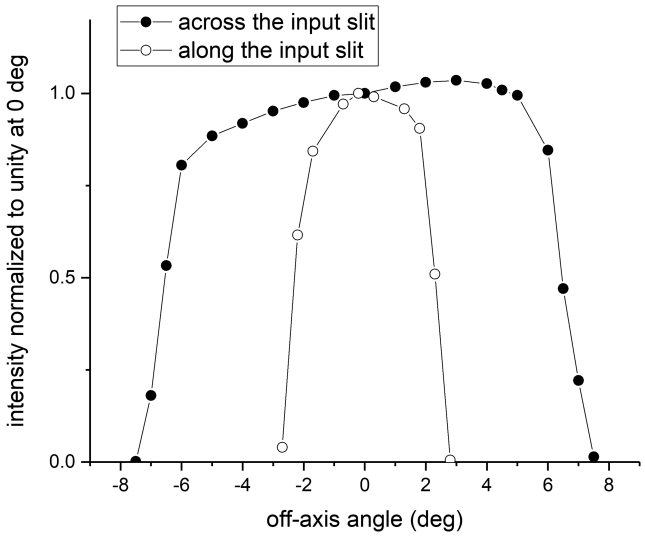

Figure 7. Angular response of the USB-650 Red Tide spectrometer measured on two axes.

LED, 30 ± 9 per cent. Normally, the spectra should go to shorter wavelengths to allow for a proper LED diagnostic. Therefore, we have taken a full spectrum ranging from 350 to 1000 nm and used it in the numerical inversion. However, Figs 5 and 6 are presented on the same spectral interval for ease of comparison. The composition of lighting technologies we identified in Kagran in 2018 differs from that which Puschnig et al. (2014) found at Vienna University Observatory, 6 years before our experiment. However, Vienna had already started the process of street-lighting modernization planning that will replace nearly 50,000 of the approximately 154,000 streetlights with fully shielded 4000 K LEDs by the end of 2020. It has to be pointed out that low-CCT LEDs (2200–2700 K) can be tolerated better than high-CCT LEDs (4000–5000 K) owing to lower emission peaks in the blue part of the visible spectrum. The 4000+ K LEDs are certainly more harmful to animals and birds than lower-CCT LEDs (Longcore et al. 2012). The presence of LEDs in the NSB spectra we recorded is not surprising because the measurements were made at the edge of Vienna and we must expect the light types prevailing in different parts of the city to not be the same, generally.

In processing the data, we considered the following effects.

(i) Angular response of the USB-650 Red Tide spectrometer. We measured this function in laboratory conditions by positioning a point light source at a distance of 3 m from the narrow opening of the spectrometer. By operating the iPANO AllView Pro as a rotating mount, we determined the optical response of the USB-650 Red Tide spectrometer on a 2D lattice with angular spacing smaller than 1° (see Fig. 7).

(ii) For the light scattering in a turbid atmosphere with a local visibility of less than 10 km at the edge of Vienna in 2018, we estimated the aerosol optical depth to be $\tau_{A0} \approx 0.4$ at $\lambda = 500$ nm (see the relationship between the visibility and the aerosol optical depth in Wu et al. 2014). This is consistent with what Bäumer et al. (2008) found, based on the Koschmieder formula for a mixing-layer height of 2 km (see fig. 6 therein). The night-sky spectrum, uncorrected for light-scattering effects, and affected by the spectral distortion due to atmospheric light scattering, is presented in Fig. 8. The contribution to the blue edge of the visible spectrum from the above correction is apparent and highlighted with ellipses. Note

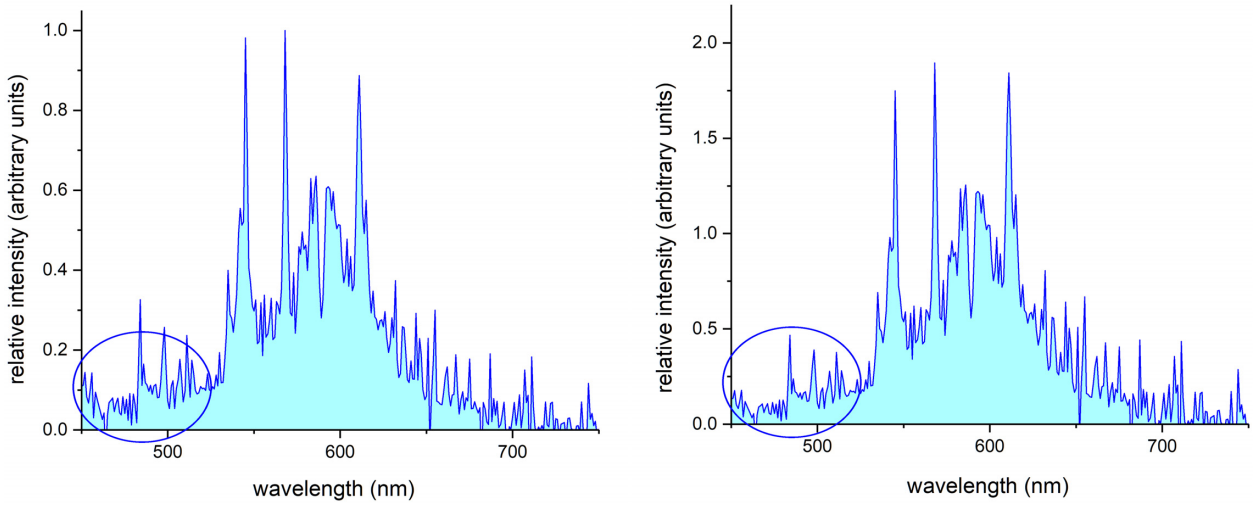

Figure 8. The NSB spectrum near Kagran (Vienna) uncorrected for light-scattering effects (left plot) versus that corrected relative to the physics introduced in Section 2 (right plot). The differences are mostly located at the blue-edge of the visible spectrum, as highlighted with ellipses.

that the dominance of light-scattering effects at the blue edge of the NSB spectrum can change when increasing the observational zenith angle (see Fig. 1).

Owing to the angular asymmetry of the instrument field-of-view (FOV, Fig. 7), we prefer the vertical orientation of the spectrometer. The acceptance angle is then as small as 4.6°, which is advantageous in theoretical modelling of the spectral distortion impacts from the light-scattering effects in the lower atmosphere (see Section 2).

There were two main changes identified in the lighting characteristics taken in 2018 (in Kagran) and 6 years earlier, in 2012 (at Vienna University Observatory): (i) the relative contribution of the FL decreased in favour of an increased contribution from the HPS, and (ii) LED lights had emerged as a new, serious light pollution because the contribution of this lighting technology to upwardly directed light is already large and, it must be noted, Vienna is still only in the early years of LED street-lighting conversion.

5 CONCLUSIONS

The spectral composition of bulk emissions from artificially lit surfaces is one of the key elements in the modelling and prediction of the negative effects that light pollution can have on astronomical observations in different spectral bands. Owing to the scattering and absorption of electromagnetic waves in the Earth's atmosphere, light of different wavelengths undergoes different amounts of optical distortion, so that the spectrum of a night sky can differ from that which has been emitted from a source of artificial light. However, because the signal detected contains information on the initial light emissions, our basic idea was to use ground-based observations of a dome of light over a city to reveal the emission spectrum of the light-pollution sources. We prefer the night-sky spectro-radiometry to be made at low elevation angles above the city because (i) elevated radiance levels of a glowing dome allow for the use of common low-cost modular spectrometers, (ii) the information content of such radiance data is high, (iii) the light transported over short optical paths does not suffer much from spectral distortion effects due to wavelength-dependent atmospheric extinction, meaning that (iv) the theoretical solution to the NSB reduces to the integral of the volume scattering coefficient for the low atmosphere (and this is an analytically treatable problem). Lowering the angular distance from a light-emitting source is also a factor that initiates a crossover from Rayleigh scattering to aerosol scattering dominance. The spectral impacts from aerosols are in general multifaceted because multiple discrete populations of aerosol particles of different origin can coexist in a local atmosphere, and the size–shape distribution functions of such particles can be highly non-trivial. However, fortunately, the low-angle scattering from spherical particles has been found to share many similarities with that from non-spherical particles (see plate 10.7 in Mishchenko, Travis & Lacis 2002); thus, the results obtained from the method we have developed here are not very dependent on the morphologies of aerosol particles. This permits the use of simple and inexpensive methods such as Mie theory or the Henyey–Greenstein approximation to model the aerosol scattering phase function.

Our validation tests have proved that the emission spectrum of a light-polluting source can be extracted from the NSB spectra. The best way to achieve this goal is to measure the spectrum of a bright dome of light over a city, or part of a city (in the case of large metropolitan areas). Close to a city or town, the light dome is very bright from the light pollution, and thus measurements can be made using low-cost spectrometers. This allows us to construct portable spectro-radiometers useful for systematic field measurements. Ocean Optics and comparable technologies are suitable for prototyping a simple device for the characterization of city emission spectra. However, near major observatories, there are no major cities – only smaller towns, often with stringent light regulations. The light domes over these towns are much dimmer than those found over major cities. The air is cleaner, with a much lower aerosol content. Spectrometers such as the Ocean Optics spectrometers are unlikely to work properly because they are too noisy. Therefore, more sophisticated optics to gather the light, and cooled detectors, are needed in dark places. With the methodology described in this paper, and the proof of concept provided, astronomers and experimentalists can build similar or more sophisticated devices and use the new algorithm we have developed (Kundracik 2019) to retrieve the cumulative spectra of whole-city lights.

The method can be used not only to determine the spectrum of light escaping a city, but also to calculate the relative contribu-

tions of different lighting technologies to bulk emissions upwards. This includes direct emissions not only from streetlights but also from other sources such as building interiors, stadiums, cars and advertisement boards, and reflected light. The method can be useful for example in the investigation of cumulative emissions and their spectral changes that result from street-lighting conversions. The current trend in streetlight optimization favours modern LED systems, which are replacing traditional technologies. However, these modern LED systems have mostly negative impacts on the skyglow. The field experiment we conducted in Kagran (part of Vienna), under clear sky conditions, indicated that the LED conversion has currently begun in Vienna, so the potential consequences to night-sky brightness have to be analysed after the conversion is completed in 2020. The ground-albedo impacts on the spectrum changes can be evaluated by incorporating the reflection spectra superimposed on the 'generic spectra'. Otherwise, the shape of the spectrum for the ground-reflected light is nearly consistent with that of the light escaping a city.

The method we have developed is applicable to arbitrary atmospheric turbidity conditions and, in conjunction with other modelling tools such as ILLUMINA (Aubé & Simoneau 2018) or SKYGLOW (Kocifaj 2018), can be used to assess the skyglow changes we can expect at observatories located near cities or towns, but also at more distant places. The theory and the method introduced in Sections 2 and 3 can also be used to systematically create an inventory of urban-emission spectra in the region of interest and monitor the changes resulting from the modernization or reconstruction of lighting systems in the selected cities.

ACKNOWLEDGEMENTS

This work was supported by the Slovak Research and Development Agency under Project No. APVV-18-0014. We are grateful to Alex Yuffa for numerous discussions and many useful comments on the manuscript.

REFERENCES

Aubé M., Roby J., Kocifaj M., 2013, Plos One, 8, e67798
Aubé M., Simoneau A., 2018, J. Quant. Spectrosc. Radiat. Transf., 211, 25
Aubé M. et al., 2016, J. Quant. Spectrosc. Radiat. Transf., 181, 11
Bäumer D. et al., 2008, Atmosph. Environ. 42, 989
Bará S. et al., 2019, Lighting Res. Technol., 51, 1092
Barentine J. C., 2019, J. Imaging, 5, 54
Barentine J. C. et al., 2018, J. Quant. Spectrosc. Radiat. Transf., 212, 10
Bohren C. F., Clothiaux E. E., 2006, Fundamentals of Atmospheric Radiation: An Introduction with 400 Problems, Wiley-VCH Verlag GmbH & Co., Weinheim
Byrd P. F., Friedman M. D., 2013, Handbook of Elliptic Integrals for Engineers and Physicists, Springer-Verlag, Berlin
Cao C., Bai Y., 2014, Remote Sens., 6, 11915
Cappa C. D. et al., 2016, Atmos. Chem. Phys., 16, 6511
Carretas F., Wagner F., Janeiro F. M., 2015, Measurement, 64, 147
Chimklai P., Hagishima A., Tanimoto J., 2004, Build. Environ., 39, 1213
Cinzano P., Falchi F. 2014, J. Quant. Spectrosc. Radiat. Transf., 139, 13
Cinzano P., Falchi F., Elvidge C. D., 2001, MNRAS, 323, 34
Davis A. B., Marshak A., 2010, Rep. Prog. Phys., 73, 026801
Dong C., 2018, J. Hydrol., 561, 573
Duriscoe D. M. et al., 2014, Light. Res. Technol., 46, 35
Falchi F. et al., 2016, Sci. Adv. 2, e1600377
Fu Q., Thorsen T. J., Su J., Ge J. M., Huang J. P., 2009, J. Quant. Spectrosc. Radiat. Transf., 110, 1640
Fukushima T., 2011, J. Comput. Appl. Math., 235, 4140
Haeffelin M. et al., 2012, Boundary-Layer Meteorol., 143, 49
Hanafy M. E., Roggemann M. C., Guney D. O., 2014, J. Opt. Soc. Am. A, 31, 1312
Horvath H., 2014, J. Quant. Spectrosc. Radiat. Transf., 139, 3
Kerola D. X., 2006, MNRAS, 365, 1295
Kocifaj M., 2007, Appl. Opt. 46, 3013
Kocifaj M., 2011, Appl. Opt. 50, 2493
Kocifaj M., 2017, Optica, 4, 255
Kocifaj M., 2018, J. Quant. Spectrosc. Radiat. Transf., 206, 260
Kocifaj M. et al., 2019, PNAS, 116, 7712
Kocifaj M., Kómar L., 2016, MNRAS, 458, 438
Kocifaj M., Solano-Lamphar H. A., 2016, PASP, 128, 124001
Kokhanovsky A. A., Zege E. P., 1997, J. Aerosol Sci., 28, 1
Kundracik F., 2019, Spectrum Analyser, Available at: http://davinci.fmph.uniba.sk/~kundracik1/SpectrumAnalyser/
Kyba C. C. M. et al., 2013a, Sci. Rep., 3, 1835
Kyba M. et al., 2013b, in Cahalan R. F., Fischer J., eds, Radiation Processes in the Atmosphere and Ocean. AIP Publishing, Melville, New York, p. 568
Li J., Barker H., Yang P., Yi B., 2015, J. Geophys. Res., 120, 12128
Li W., Tan D., Xu J., Wang S., Chen Y., 2019, Opt. Express, 27, 16047
Longcore et al., 2012, J. Exp. Zool. A Ecol. Integr. Physiol., 329, 511
Louedec K. et al., 2012, Eur. Phys. J. Plus, 127, 97
Mayer B., Kylling A., 2005, Atmos. Chem. Phys., 5, 1855
Mishchenko M. I., Travis L. D., Lacis A. A., 2002, Scattering, Absorption, and Emission of Light by Small Particles, Cambridge University Press, Cambridge
Moosmüller H., Ogren J. A., 2017, Atmosphere, 8, 133
Narisada K., Schreuder D. 2004, Light Pollution Handbook, Springer, Dordrecht
Novák T., Sokanský K., Diviš D., 2011, in Leonowicz Z., ed, 10th Int. Conf. on Environment and Electrical Engineering, EEEIC.EU 2011 – Conf. Proc., IEEE, Institute of Electrical and Electronics Engineers, Piscataway NJ USA, p. 2032
Pepijn J. et al., 1999, J. Geophys. Res., 104, 2253
Puschnig J., Posch T., Uttenthaler S., 2014, J. Quant. Spectrosc. Radiat. Transf., 139, 64
Rozanov V. V., Rozanov A. V., Kokhanovsky A. A., Burrows J. P. 2014, J. Quant. Spectrosc. Radiat. Transf., 133, 13
Solano-Lamphar H. A., 2018, J. Quant. Spectrosc. Radiat. Transf., 211, 35
Tapia Ayuga C. E., Zamorano J., 2018, J. Quant. Spectrosc. Radiat. Transf., 214, 33
Tapia Ayuga C. E. et al., 2019, Available at: https://guaix.fis.ucm.es/lamps_spectra
Wu J., Luo J., Zhang L., Xia L., Zhao D., Tang J., 2014, J. Geophys. Res., 119, 13370
Yang X., Li Y., 2015, Build. Environ., 90, 146

This paper has been typeset from a Microsoft Word file prepared by the author.